



## Effect of IMF $B_y$ on thermospheric composition at high and middle latitudes:

### 2. Data comparisons

Thomas J. Immel,<sup>1</sup> Geoff Crowley,<sup>1</sup> Chris L. Hackert,<sup>2</sup> John D. Craven,<sup>3</sup> and Ray G. Roble<sup>4</sup>

Received 9 August 2005; revised 11 April 2006; accepted 16 May 2006; published 19 October 2006.

[1] The strength and orientation of the interplanetary magnetic field (IMF) has a strong effect on the high-latitude plasma convection pattern, thereby influencing the speed and direction of polar thermospheric winds. The possibility of similar IMF control over the compositional response of the thermosphere during geomagnetic disturbances has not been fully investigated. This study finds that the y-component of the IMF (IMF  $B_y$ ) exerts significant control over the development and subsequent equatorward transport of composition disturbances during periods of heightened geomagnetic activity. This is determined using the NCAR-TIMEGCM to simulate the thermospheric conditions during the first 3 weeks far-ultraviolet (FUV) imaging operations of the Dynamics Explorer 1 (DE-1) mission in 1981. The images reveal changes in the relative thermospheric column abundance of O versus  $N_2$  ( $\Sigma O/N_2$ ). These changes are reproduced by the model, incorporating variable IMF strength and orientation as inputs. It is found that simple reversal of IMF  $B_y$  leads to subsequent changes in  $\Sigma O/N_2$  at middle latitudes by as much as 30%. This is a manifestation of the effect identified in the companion to this report (Crowley et al., 2006). The study confirms the hypothesis of Immel et al. (1997) that IMF- $B_y$  effects on middle-latitude thermospheric composition are important, though more complex than expected. Contrary to previous predictions, early morning local times are shown to be more likely to suffer large decreases in  $\Sigma O/N_2$  when  $B_y$  is negative. However, the overall magnitude of high-latitude Joule heating is found to be greater when  $B_y$  is positive.

**Citation:** Immel, T. J., G. Crowley, C. L. Hackert, J. D. Craven, and R. G. Roble (2006), Effect of IMF  $B_y$  on thermospheric composition at high and middle latitudes: 2. Data comparisons, *J. Geophys. Res.*, *111*, A10312, doi:10.1029/2005JA011372.

### 1. Introduction

[2] Heating of the upper atmosphere by the polar aurorae is a phenomenon first posited by *Birkeland* [1913]. It was more than 40 years later, with the first direct measurements of upper-atmospheric conditions, when these effects could finally be quantified. Early in the Space Age, careful study of the variation in satellite orbits clearly established the association of increased atmospheric drag with heightened solar activity and the occurrence of geomagnetic storms [*Jacchia*, 1959]. Since then, other satellites have employed a range of techniques to quantify the compositional variations and other effects driven by auroral heating. These include the Ogo-4 and -6 satellites [*Meier and Prinz*, 1971; *Strickland and Thomas*, 1976], the S3-4 satellite [*Conway et*

*al.*, 1988], the ESRO satellites [*Pröls*, 1980], and Atmospheric and Dynamics Explorer satellites [*Burns et al.*, 1995]. Most of these carried mass spectrometers for direct in situ measurements of the neutral composition and density. Of these early missions the Ogo-6 and S3-4 satellites were also equipped with far-ultraviolet (FUV) sensors to infer neutral composition via emission brightnesses of neutral atmospheric species.

[3] In the past 3 decades the means of retrieving upper-atmospheric composition from FUV observations has been well developed. Whereas satellites once made photometric measurements in low-Earth orbit, researchers now obtain global-scale images from platforms at several  $R_E$  altitude using photometric, filtered CCD, and more recently, spectrographic imaging techniques [*Mende et al.*, 2003; *Christensen et al.*, 2003]. Missions that are so instrumented usually focus on FUV auroral observations, but measurements of the dayside emissions of atomic oxygen at 130.4 and 135.6 nm can usually be adopted for thermospheric studies. In the case described in this report, images of the terrestrial emissions of O I at 130.4 nm came from the University of Iowa Spin-Scan Auroral Imager on Dynamics Explorer 1 (DE-SAI) that became operational on 22 September 1981 [*Frank et al.*, 1981]. The imager obtained these global-scale images in

<sup>1</sup>Space Sciences Laboratory, University of California, Berkeley, California, USA.

<sup>2</sup>Southwest Research Institute, San Antonio, Texas, USA.

<sup>3</sup>Geophysical Institute and Physics Department, University of Alaska, Fairbanks, Alaska, USA.

<sup>4</sup>National Center for Atmospheric Research, Boulder, Colorado, USA.

successive 12-min intervals from the vantage point of an elliptical orbit with an apogee altitude of 3.65 Re. The DE-SAI had one FUV channel with several selectable filters, one of which (2) produced images of mainly 130.4-nm emissions. All of the other filters either suppressed 130.4-nm emissions or accepted geocoronal emissions at 121.6 nm, so not all operating modes of the instrument are amenable to thermospheric studies.

[4] Early analyses of the dayside terrestrial emissions observed by DE-SAI revealed large-scale decreases in O I brightness which occurred after periods of significant geomagnetic activity [Frank and Craven, 1988]. At the time of those observations, it was well known that high-latitude heating produced thermospheric composition disturbances [Prölss and Roemer, 1987] and concomitant decreases in O I brightness [cf. Meier 1970]. The relation between the composition variations and decreased FUV emissions had been confirmed using numerical simulations of the radiative transfer of FUV emissions [Meier and Prinz, 1971; Strickland and Thomas, 1976]. It was, however, the first study to provide a global view of the distribution of high-latitude Joule heating effects that had propagated to middle latitudes on the dayside.

[5] Studies of the thermospheric effects of high-latitude heating as observed by DE-1 focused on these depletions of O I airglow brightness as related to changes in  $\Sigma\text{O}/\text{N}_2$ , the ratio of O to  $\text{N}_2$  throughout the column of air emitting FUV radiation. Craven *et al.* [1994] quantitatively determined the magnitude and motion of a large-scale airglow depletion observed after the 22 October 1981 magnetic storm. Their study used the empirical dayglow models later described by Nicholas *et al.* [1997] and Immel *et al.* [2000] to establish a baseline for comparison with observed brightnesses. Gladstone [1994] and Meier *et al.* [1995] reported success in adapting first-principles radiative transfer models to global imaging applications for similar analyses. Several more studies have focused on the ionospheric effects related to thermospheric storms [e.g., Prölss and Craven, 1998; Strickland *et al.*, 2001b; Immel *et al.*, 2001] and on the global storm effects in general [e.g., Drob *et al.*, 1999].

[6] Further investigation of the DE-SAI images found indications of the importance of the high-latitude thermospheric wind pattern in the development of middle-latitude decreases in  $\Sigma\text{O}/\text{N}_2$  [Immel *et al.*, 1997]. In particular, an apparent relation to the  $y$ -component of the interplanetary magnetic field (IMF  $B_y$ ) was identified. That study provides impetus to the research undertaken as part of this report. To date, no atmospheric general circulation simulations have been performed to test the hypothesis of IMF- $B_y$  influence on the development of thermospheric composition perturbations at middle latitudes. The companion to this report presents the first initial tests of the  $B_y$ -effect hypothesis, confirms the effect is important, and provides an initial characterization of the effect under steady-state high-latitude inputs. This paper completes the study by testing the hypothesis for the actual geomagnetic and solar-wind conditions present during the times investigated by Immel *et al.* [1997].

[7] Both of these studies rely on the National Center for Atmospheric Research (NCAR) Thermosphere-Ionosphere-Mesosphere-Electrodynamics General Circulation Model (TIMEGCM) to simulate the upper atmospheric conditions during the first 3 weeks of the Dynamics Explorer mission

for comparison with the global-scale images. In this report, the validity of the GCM runs is assessed with comparisons to the DE-SAI images. Once the level of confidence in the model is determined, a study of the role of the high-latitude neutral circulation in the development of middle-latitude thermospheric disturbances is undertaken. In this manner, the research both investigates the capability of the model for reproducing the observed thermospheric disturbances and the origin of high-latitude influence on middle-latitude thermospheric variability.

## 2. Global FUV Observations

[8] In full-Earth imaging mode, the DE-SAI FUV imager obtained a  $120 \times 150$  pixel image in 12 min. In obtaining these images, the instrument used a single photometer whose field-of-view was directed with a mirror at small angles above and below the spin plane of the DE-1 satellite in 0.25 degree steps. Series of pixels were produced by integrating photometer counts in 0.23 degree steps of satellite rotation angle as the field-of-view swept through the nadir [Frank *et al.*, 1981]. The 123-nm wideband filter was used frequently throughout the mission, providing images where the response of the photometer is primarily due to O I emissions at 130.4 nm. This emission originates in the aurora and also from the sunlit thermosphere, where nominal per-pixel counting rates for dayside observations are generally in the 20–100 counts/pixel range, depending mainly on the solar zenith angle at each observed location on Earth.

[9] The DE-SAI imaging data presented in this report are processed to produce 1-hour summaries of the FUV observations with improved counting statistics. Up to five images are combined for each hour of imaging by coaddition of pixel counting rates in a  $0.5^\circ \times 0.5^\circ$  grid of geographic latitude and longitude. Images are excluded if they show evidence of radiation-belt contamination of the photometer signal. Once average hourly counting rates are determined, average quiet-time background counting rates are also determined, using the method of Immel *et al.* [2000]. Percent differences from this quiet-time dayglow model are then determined. Application of the model effectively removes brightness variations due to observational geometry and solar zenith angle. Further corrections for solar EUV flux variations use daily measured solar 10.7-cm radio flux as a proxy for solar EUV. DE-1 images in this and the accompanying report [Crowley *et al.*, 2006] are only shown after the application of this processing technique.

## 3. TIMEGCM Model Runs and Analysis Technique

[10] The NCAR TIMEGCM is a fully coupled first-principles model of the upper atmosphere that predicts winds, temperatures, and ion and neutral concentrations on surfaces of constant pressure from 900 to  $4.3 \times 10^{-6}$  Pa [Roble and Ridley, 1994]. This range of pressures corresponds approximately to an altitude range of 30 to 600 km. Inputs that directly affect neutral composition are solar heating, high-latitude particle precipitation, and magnetospheric convection electric fields. These inputs are parameterized and controlled by the externally measured solar radio flux

at 10.7 cm, the precipitating hemispheric auroral power ( $H_p$ ), and the cross-polar-cap electric potential ( $\Phi$ ), respectively. The daily solar radio flux values are provided by the Canadian National Research Council, while the distribution of precipitating auroral power is calculated from passes of NOAA satellites [Fuller-Rowell and Evans, 1987]. The high-latitude electric fields are determined using a Heelis electric potential pattern [Heelis et al., 1982] that produces a two-celled pattern with IMF dependence. IMF data from the Vector Helium Magnetometer aboard ISEE-3 [Frandsen et al., 1978] with 5-min resolution are used to control the Heelis model. Data gaps are filled in with 15-min averages from the OMNI 2 database maintained at NASA Goddard Space Flight Center, which incorporates all other available IMF data, including measurements from the IMP-8 spacecraft, for example.

[11] In this study, the TIMEGCM is used to simulate the development of middle-latitude thermospheric composition perturbations observed by the DE-SAI instrument and to test the importance of  $y$ -component of the IMF in the development of these perturbations. It is run with the above-specified inputs over the time frame beginning on Day 263 (20 September), 1981 and finishing at the end of Day 284 (11 October). This interval covers the two event intervals beginning on Days 267 and 280 discussed by *Immel et al.* [1997] and noted by *Crowley et al.* [2006]. Starting the run several days before the first event interval and running it continuously on through the second interval allows the TIMEGCM to best simulate the atmospheric conditions existing prior to the onset of significant magnetic activity.

[12] The main run is accompanied by a quiet run, in which the inputs are set to low values ( $H_p = 3$  GW,  $\Phi = 30$  kV, IMF  $B_y = 0$  nT) and only the solar flux is allowed to vary realistically. This provides a background model atmosphere where diurnal and seasonal solar flux variations are the sole drivers of variability in global thermospheric composition. The seasonal change is quite significant over the 3 weeks of the full run, and it is insufficient to compare model outputs to a single, UT-dependent quiet atmosphere, as may be done for shorter study intervals [cf. *Immel et al.*, 2001]. This background run is used as a baseline for quantifying the variations that the main TIMEGCM run predicts in thermospheric composition.

[13] A third TIMEGCM run is also performed with the correct high-latitude inputs, but the  $y$ -component of the IMF is multiplied by  $-1$ . This change will have its greatest effect when the magnitude of IMF  $B_y$  is large and geomagnetic activity is generally high. Comparison of this run with the main run described above effectively indicate when and where IMF  $B_y$  has the greatest influence on thermosphere neutral winds and composition.

[14] In making comparisons with FUV brightness, the most important modeled quantities are the thermospheric column abundance of atomic oxygen and molecular nitrogen. As noted earlier, for the selected filter (2) the 130.4-nm emission of thermospheric O I dominates the DE-SAI response [Meier et al., 1995]. The terrestrial 130.4-nm emission has two sources of excitation; resonant excitation by the bright solar O I line and in situ collisional excitation of O I by terrestrial photoelectrons in the 10 eV range. The total emission rate is also modulated in two ways, first in a manner dependent the abundances of FUV absorptive O<sub>2</sub> in

the lower thermosphere [Strickland and Thomas, 1976; Strickland and Jr., 1977], and second by competition of O with N<sub>2</sub> for available photoelectron energy [Parish et al., 1994]. Both of these effects are strongest in the lower portion of the radiating column of gas (below  $\sim 160$  km). Because the density profiles of N<sub>2</sub> and O<sub>2</sub> are similar in the lower thermosphere, these species can be considered to covary under the effects of heating. Selecting the dominant species N<sub>2</sub> as the reference, the O I 130.4-nm emission brightness shares a close relationship with the ratio of the column densities of O and N<sub>2</sub>, allowing retrieval of  $\Sigma O/N_2$  with an uncertainty on the order of  $\pm 10\%$  [Strickland et al., 1999].  $\Sigma O/N_2$  therefore is the parameter extracted from the TIMEGCM model runs for direct comparisons with the FUV imaging.

[15] Since the FUV brightness is directly related to  $\Sigma O/N_2$ , there is no need to convert FUV brightnesses to  $\Sigma O/N_2$  using any forward modeling technique [cf. *Strickland et al.*, 2001a]. They are rather presented as percent differences from quiet-time FUV brightness levels, as described in the previous section. Likewise, the  $\Sigma O/N_2$  determined from the TIMEGCM runs is not converted to FUV brightness. As the relationship between  $\Sigma O/N_2$  and O I-produced FUV emissions is very nearly linear, the only correction necessary for one-to-one comparisons of percent differences of FUV brightness and  $\Sigma O/N_2$  is a single multiplicative factor and a fixed offset. Neither of these mathematical corrections would have any effect on the calculation of correlation coefficients, or other methods of comparing the FUV measurements and TIMEGCM results, and are therefore not applied. Much as the FUV PD images were determined, the percent changes in the TIMEGCM  $\Sigma O/N_2$  are determined by comparing values from the main run to those established in the fixed-low-activity run.

#### 4. Magnetic Activity During the Day 264–284, 1981, Study Period

[16] The Auroral Electrojet (AE) indices for the first 20 days of DE-SAI imaging are shown with the pertinent IMF parameters for the period in Figures 1 and 2. Enhancements in the AE index are indicative of increases in auroral currents driven by geomagnetic disturbances. The aeronomical impact of the geomagnetic activity in the period from days 267 through 272 of 1981 was the topic of a study by *Strickland et al.* [2001a]. The current investigation focuses on the days at the beginning of the Strickland et al. period, and on a time of significant activity 10 days after the end of their study period. These are times when the IMF  $B_y$  component was strong.

[17] The  $y$ - and  $z$ -components of the IMF also shown in Figures 1 and 2 are from the National Space Science Data Center OMNI database, where the time base is estimated magnetopause-arrival time. In the top panel of each 10-day plot, a solid line shows the  $z$ -component of the field (in geocentric solar magnetic (GSM) coordinates), and a grey-shaded histogram shows the total magnetic field strength. The bottom panel shows the GSM  $y$ -component of the field. Significant excursions of the  $z$ -component into negative values occur repeatedly between Days 265 and 270, as well as from 280 onward. These times correspond to the greatest observed dayglow depletions at middle latitudes. During

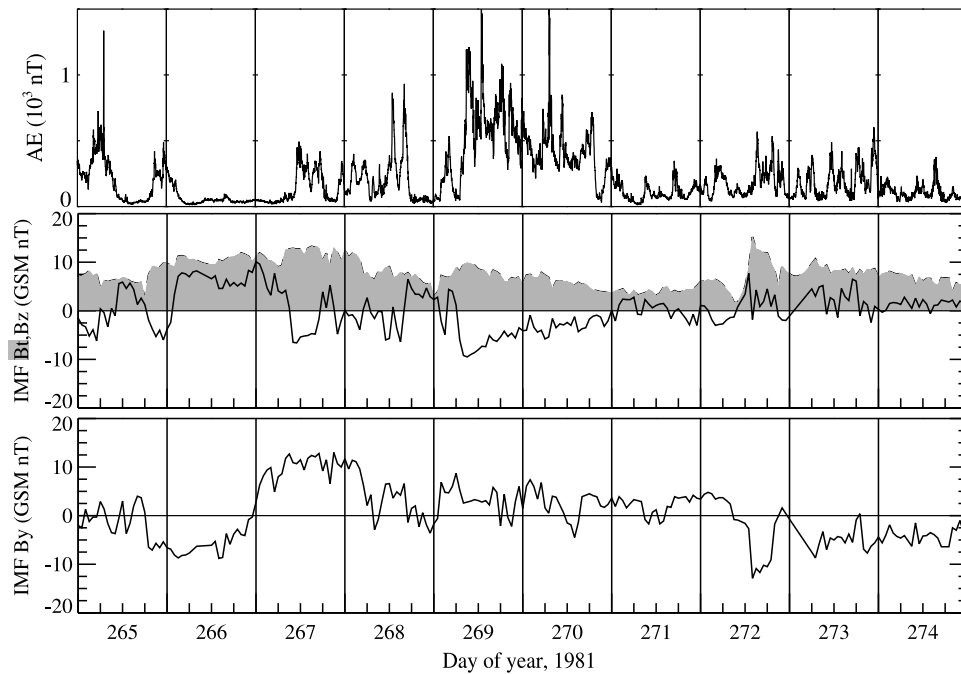


**Figure 1.** The AE indices and IMF parameters for the first 10 days of the study period.

these times, particularly on Days 267, 281–282, and 284, the IMF y-component was consistently large and positive. There are also strong negative excursions of the  $B_y$  component on Days 266 and 272.

## 5. TIMEGCM Validation: $\Sigma O/N_2$ Versus DE-1 FUV Observations

[18] In this section, the DE-SAI PD images are compared directly to the TIMEGCM  $\Sigma O/N_2$ , as described in section 1. Green contours indicate regions where 20% reductions in

either 130.4-nm emissions or TIMEGCM  $\Sigma/N_2$  are found. The goal of this section of the report is to provide a qualitative assessment of the degree to which the neutral atmosphere in the TIMEGCM reflects the actual conditions reflected in the DE-SAI images. Only with agreement between the TIMEGCM and DE-SAI images can we proceed to identify the sources of heating effects.

### 5.1. Days 267–268

[19] The images in Figure 3 show a gradually increasing buildup of Joule heating effects on the thermospheric

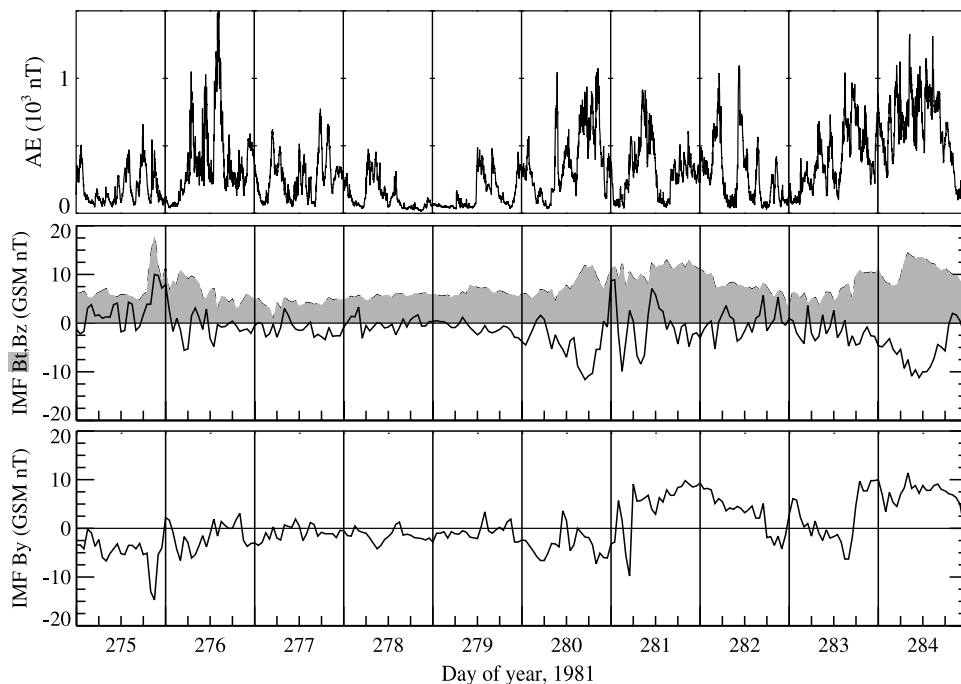


**Figure 2.** The AE indices and IMF parameters for the last 10 days of the study period.

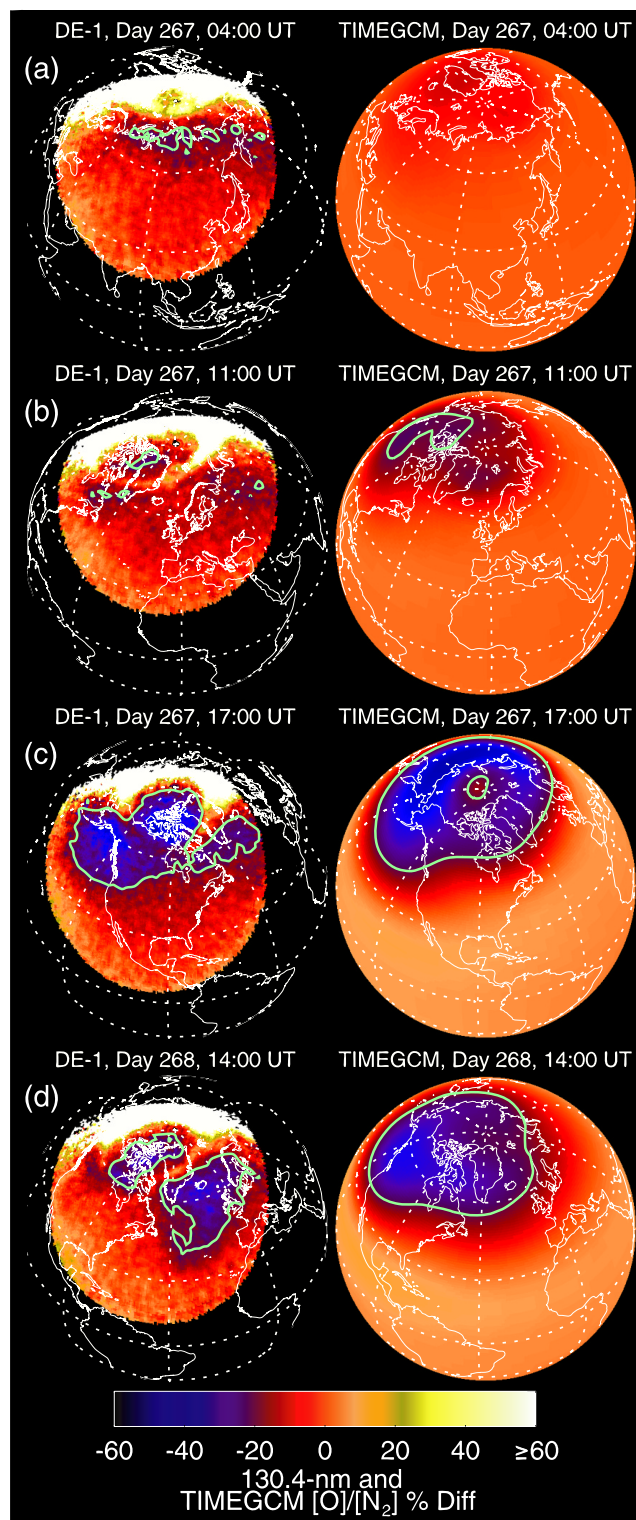


**Figure 3.** Percent difference (PD) in 130.4-nm brightness and TIMEGCM  $\Sigma O/N_2$  maps for the Day 267–268 period of interest.

composition over several hours of time. Images obtained over three consecutive DE-1 orbits on Day 267 are shown to the left in Figures 3a, 3b, and 3c. Initially at 0400 UT, no disturbance appears in either the DE-SAI image (at left) or the TIMEGCM (to the right). At 1100 UT, no large-scale

airglow depletions were observed, although there is a  $\sim 10$ – $15\%$  decrease generally on the dayside, reaching  $-30\%$  in the Russian and Canadian sectors. The auroral activity is high at this moment ( $AE \simeq 500$  nT), and the signature of the auroral oval is visible over the Arctic Ocean and Greenland. The TIMEGCM run starts to show significant decreases in  $\Sigma O/N_2$  at high latitudes, most significantly over the North American sector. At this time this sector is still on the nightside, but if the TIMEGCM is correct then reduced FUV brightnesses should be apparent in this sector once it rotates to the dayside. Six hours later, DE-1 obtained images of the North American sector as it approached noon local time, a period discussed at length by *Immel et al.* [1997] and shown for reference in the companion to this report [*Crowley et al.*, 2006]. The FUV and TIMEGCM PD images for this period are shown in Figure 3c. Indeed, the TIMEGCM and FUV images show a remarkably similar effect, a decrease in FUV brightness (and  $\Sigma O/N_2$ ) throughout the high northern latitudes, extending to middle latitudes in the Northern Pacific and western North American sectors. The contours of the FUV and TIMEGCM quantities are practically identical. Significantly, these conditions developed during a period of very strongly positive IMF  $B_y$ . With the knowledge that the TIMEGCM agrees very well with the observations, the influence of the IMF component will be further investigated in a later section of this report. The notable difference between the TIMEGCM and the DE-1 observation that develops by 1400 UT on Day 268 (Figure 3d) is also further discussed.

## 5.2. Days 279–281

[20] The imaging times shown in Figures 4a–4d were also a focus for *Immel et al.* [1997], beginning at 1800 UT on day 279 (Figure 4a). The FUV image shows that increases in magnetic activity (cf. Figure 2) do not result in reductions of  $\Sigma O/N_2$  at middle latitudes. The TIMEGCM is in agreement with this observation. Stronger magnetic activity occurred beginning on day 280, when the  $y$ -component of the IMF was predominantly negative. This is the case for the two FUV images obtained around 1300 and 2100 UT on Day 280 in Figures 4b and 4c, respectively. The TIMEGCM shows a significant effect of high-latitude heating at 1300 UT, with  $\Sigma O/N_2$  extending into the morning sector, an effect that is just beginning to appear in the FUV images. By 2100 UT, this reduction in TIMEGCM  $\Sigma O/N_2$  has corotated toward the afternoon sector. Though it lags somewhat behind the afternoon reduction in FUV brightness seen in the DE-SAI image over Canada, it explains the source of that reduction in brightness as a composition disturbance that has corotated from the morning sector. After these images were obtained, IMF  $B_y$  changed to positive values beginning early on Day 281. The last data-model comparison at 1700 UT on Day 281 (Figure 4d) shows an excellent overall correspondence between the FUV signature and TIMEGCM. Each shows the clear extent of heating effects out of the polar cap and into the morning sector.

[21] The qualitative assessment of this section is that the TIMEGCM provides a remarkably accurate simulation of the atmospheric conditions during the times of interest. With the good match between the DE-SAI images and TIMEGCM predictions of thermospheric conditions, we proceed in our analysis with confidence.

## 6. Modeled IMF By Effect

[22] In the companion to this report, *Crowley et al.* [2006] described numerical experiments showing that the orientation of IMF  $B_y$  during periods of high-latitude heating influenced the resultant  $\Sigma O/N_2$  perturbations on a global scale. Using steady model inputs, it is found that greater depletions of  $\Sigma O/N_2$  are maintained at middle latitudes in the morning sector under  $B_y < 0$  conditions. Conversely, during periods in which  $B_y > 0$ , depletions in  $\Sigma O/N_2$  at high latitudes were found to be more significant. These simulations suggested that more significant reductions in  $\Sigma O/N_2$  at middle latitudes should be expected under  $B_y < 0$  conditions, contrary to the conclusions of *Immel et al.* [1997]. The realistic, time-varying simulations presented in this report permit investigation of the temporal development of the thermospheric disturbances on the days of particular interest for their large values of IMF  $B_y$ .

### 6.1. Day 267-268: Strong $B_y$ Positive

[23] The first period of obviously strong IMF- $B_y$  influence began on Day 265 and continued into Day 268. Successive excursions of  $B_z$  to negative values on Days 265 and 267 (reaching values between  $-5$  and  $-7$  nT each time (see Figure 1)) drove increased high-latitude energy inputs, whose effects were noted in both the DE-SAI images and the TIMEGCM model atmosphere (cf. section 5.1). The  $y$ -component also varied, beginning around 0 nT at the start of Day 265, with a trend toward more negative values until early on Day 266, when  $B_y$  reached  $-9$  nT. Thereafter, IMF  $B_y$  tended toward positive values, reaching 0 nT by the end of day 266 and  $+10$  nT at 0900 UT on day 267. At this time on day 267,  $B_z$  turned significantly negative, immediately producing heating effects at high latitudes (see AE index in Figure 1). At 1700 UT when DE-1 images are available, the decrease in  $\Sigma O/N_2$  is evident, as seen in Figure 5. This raises the following question: Did the  $y$ -component of the IMF play a significant role in the transport of disturbed parcels of atmosphere into the North American sector?

[24] This question is answered by comparing the Truth TIMEGCM run against the  $B_y$ -reversed run. If the IMF  $B_y$  component plays a significant role in the development of middle-latitude composition disturbances, it will be clear in the difference of the  $\Sigma O/N_2$  of the two simulations. Percent differences of the  $B_y$ -reversed run from the Truth run are calculated in a manner similar to that used earlier to determine departures of the original TIMEGCM run from the quiet-time run. The formula  $PD = (Reverse - Truth) / Truth \times 100\%$  is used in all the figures that follow.

[25] The  $\Sigma O/N_2$  from both the Truth and  $B_y$ -reversed runs are shown in Figure 5 at 1700 UT on Day 267, accompanied by the DE-1 PD images obtained at the same time (as also shown in Figure 3c). There is a clear difference in the morphology and depth of the  $\Sigma O/N_2$  perturbation, with the Truth run indicating a stronger departure from quiet-time levels at high latitudes (yellow-white), and a weaker reduction in  $\Sigma O/N_2$  in the morning sector (blue). Stated differently, the  $B_y$ -reversed run ( $B_y < 0$ ) produced 15% greater depletions in thermospheric  $\Sigma O/N_2$  in the North American (morning) sector than did the Truth run ( $B_y > 0$ ). This particular observation agrees with the conclusions of *Crowley et al.* [2006], that IMF  $B_y < 0$

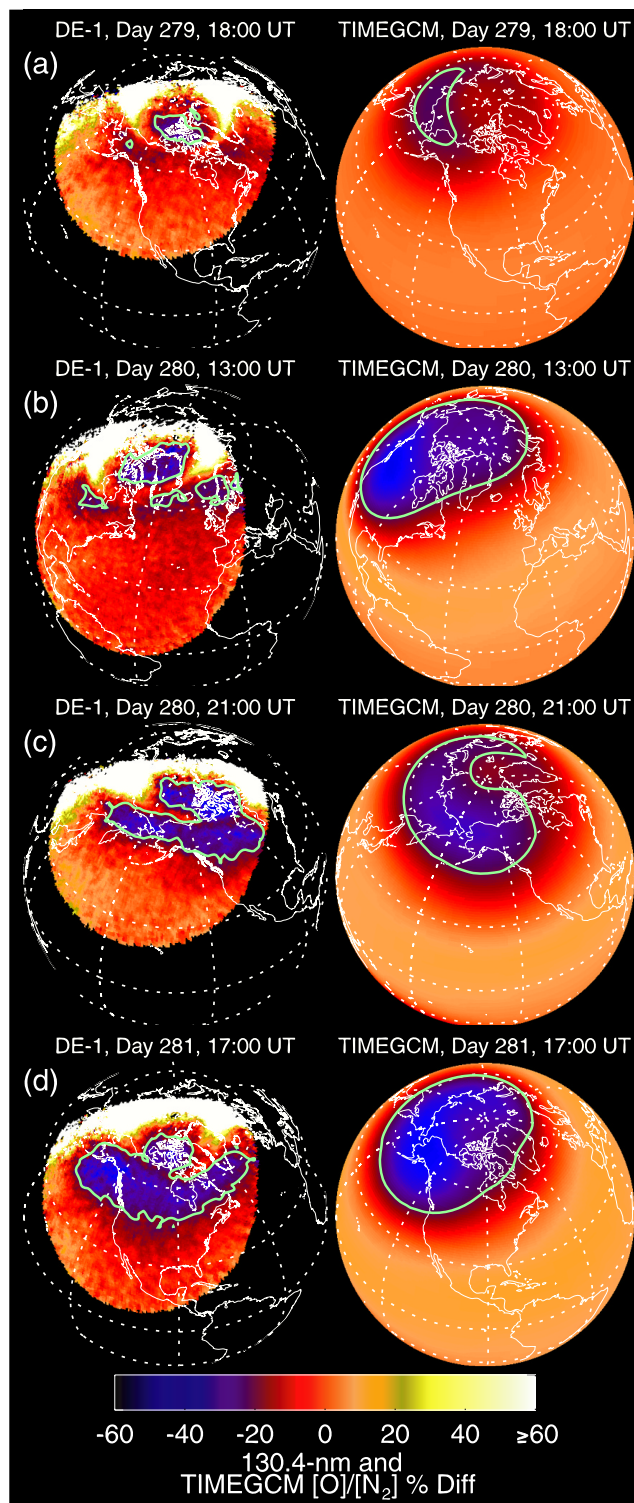


**Figure 4.** PD in 130.4-nm brightness and TIMEGCM  $\Sigma O/N_2$  maps for the Day 279–281 period of interest.

conditions during periods of enhanced activity favor the development of morning-sector  $\Sigma O/N_2$  depletions.

[26] To track the development of the features observed in Figure 5, Figure 6 shows the differences between the  $B_y$ -reversed and Truth runs at 2-hour intervals for all of Day 267. Differences between the model runs are seen to grow

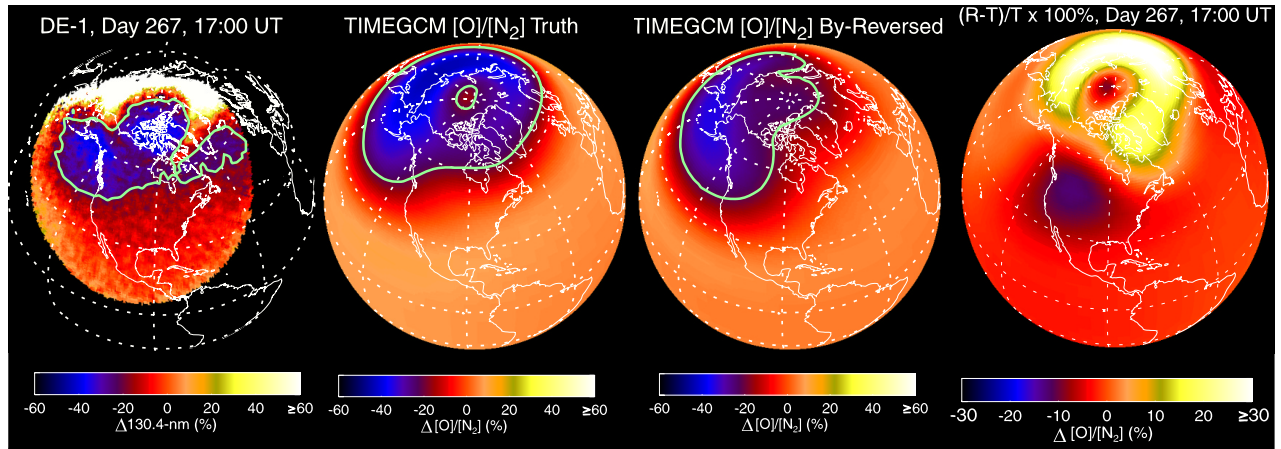


**Figure 5.** Effect of IMF-By reversal on TIMEGCM  $[O/N_2]$ . From left to right, the DE-1 percent difference image from 1700 UT, Day 267 is shown with two TIMEGCM  $\Sigma O/N_2$  PD images for the Truth and By-reversed runs. The rightmost frame shows the percent differences of the By-reversed run from the Truth run. The color scale represents  $\pm 60\%$  in all the images except the rightmost frame, where the range is reduced to  $\pm 30\%$ .

from 0600 UT onward, under the influence of a strong IMF  $y$ -component that is consistently around  $+10$  nT. The growth of differences becomes more rapid with the southward turn of  $B_z$  after 0800 UT, particularly at high latitudes on the dayside and in the morning sector at middle latitudes. From 1200 UT onward, the light-colored region indicates that the Truth run ( $B_y > 0$ ) produces 30% stronger decreases in  $\Sigma O/N_2$  over an increasingly large area at high latitudes. At the same time, the By-reversed run ( $B_y < 0$ ) consistently produces 20–30% greater reductions in  $\Sigma O/N_2$  in a roughly  $1500 \text{ km}^2$  region at subauroral latitudes in the morning sector. [27] This middle-latitude region of enhanced thermospheric perturbation subcorotates, shifting from eastern

Canada at 1200 UT to west of Alaska and Siberia by 2200 UT. It can therefore be said that during this event, high-latitude convection continuously affected the neutral composition in the morning sector at middle latitudes. This is the first finding of this effect, though the global changes in thermospheric neutral winds effected by variations in high-latitude neutral wind patterns was earlier described by *Rees et al.* [1986]. That phenomenon was invoked by *Immel et al.* [1997] to explain the apparent effect of IMF  $B_y$  on middle-latitude thermospheric composition disturbances cannot be undertaken simply in the context of the local time sector into which the high-

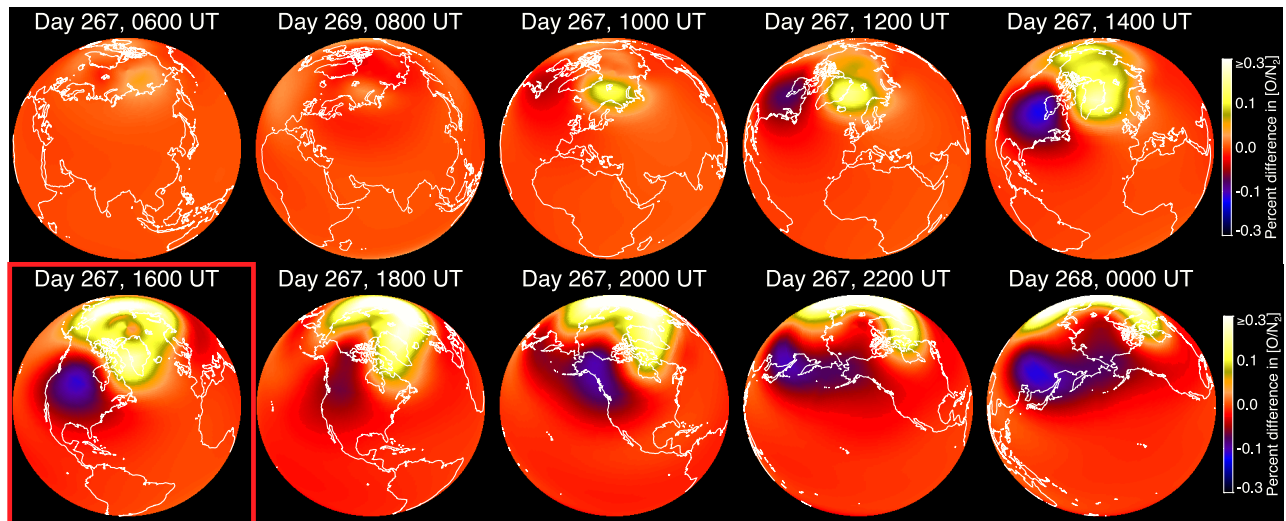


**Figure 6.** Development of differences between the By-reversed and Truth TIMEGCM runs on Day 267. Locations of decreases in  $\Sigma O/N_2$  in the By-reversed run that are stronger (weaker) than in the Truth run are indicated by negative (positive) percents. After 1200 UT, the By-reversed run produces stronger depletions in the North American sector than does the normal run, with much weaker depletions of  $\Sigma O/N_2$  in the auroral zone. The TIMEGCM output from the time closest to the DE-1 PD imaging period described in Figure 3c is framed in a red box.

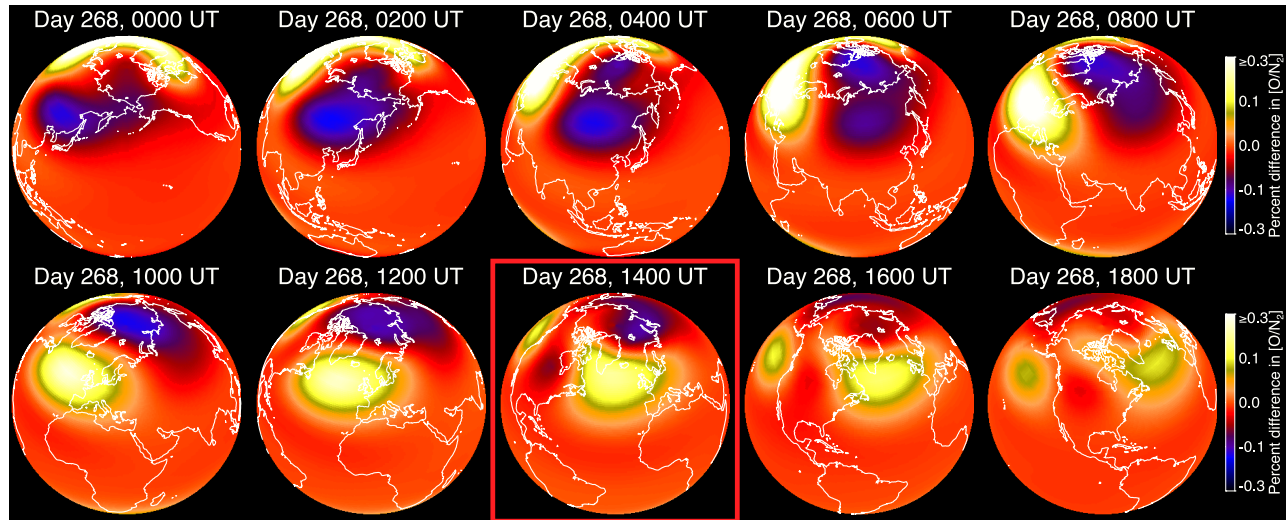


**Figure 7.** Development of differences in TIMEGCM runs for normal and By-reversed conditions on Day 268. Locations of decreases in  $\Sigma\text{O}/\text{N}_2$  in the By-reversed run that are stronger (weaker) than in the Truth run are indicated by negative (positive) percents. In this 18-hour period, the region of stronger  $\Sigma\text{O}/\text{N}_2$  depletion produced in the Truth run on Day 267 migrates to the dayside, while the region of stronger  $\Sigma\text{O}/\text{N}_2$  depletion in the By-reversed run appears to migrate into the polar cap. The TIMEGCM output from time closest to the DE-1 PD imaging period described in Figure 3d is framed in a red box.

latitude neutral winds most effectively advect the thermospheric disturbances.

[28] It is instructive to follow the development of By-produced differences in  $\Sigma\text{O}/\text{N}_2$  through the next day while IMF  $B_y$  remains strongly positive. These are shown in 2-hour steps from 0000 to 1800 UT for Day 268 in Figure 7. The first image in the sequence is identical to the last image in Figure 6. In the first 4 hours of the day, the  $\Sigma\text{O}/\text{N}_2$  values at sunlit middle latitudes in the Reversed-By run remain significantly lower than the Truth run, though this region now corotates and advances across the noon local time sector at the speed of full corotation. This region of stronger  $\Sigma\text{O}/\text{N}_2$  depletion also begins to migrate into the polar cap at 0400 UT, moving completely to high latitudes by 1000 UT. While this occurs, the large area (orange-to-white) of stronger  $\Sigma\text{O}/\text{N}_2$  decreases in the Truth run also begins to corotate, emerging onto the dayside at 0800 UT, and thereafter dominating the middle latitudes across the dayside until the differences largely disappear after 1800 UT as the level of magnetic activity and magnitude of IMF  $B_y$  are both greatly reduced. The Truth run predicts a much deeper depletion in  $\Sigma\text{O}/\text{N}_2$  in the noon local time sector at 1400 UT, when DE-1 also observes a strong depletion in the noon-to-postnoon sector (see Figure 3d).

[29] One can summarize these observations by noting three particularly striking results. First, the By-reversed run predicts that the depletion in  $\Sigma\text{O}/\text{N}_2$  seen over North America on Day 267 (Figure 5a) is not an effect attributable to  $B_y > 0$ , but rather to the effect of strongly negative  $B_z$ . Second, the high-latitude  $\Sigma\text{O}/\text{N}_2$  disturbance is much stronger and more extensive in the case of the Truth run ( $B_y > 0$ ). This leads to the third point, that this enhanced polar cap depletion eventually migrates to middle latitudes and corotates to the dayside. The TIMEGCM shows how this area of strongly depressed  $\Sigma\text{O}/\text{N}_2$  corotates into the noon sector at a time which coincides with the observation of anomalously

large afternoon  $\Sigma\text{O}/\text{N}_2$  depletion in FUV images obtained at 1400 UT. Though the TIMEGCM Truth run does not maintain the reduced  $\Sigma\text{O}/\text{N}_2$  at  $-20\%$  as the DE-SAI image suggests, the atmospheric parcels in the TIMEGCM that lie in the afternoon sector at 1400 UT on Day 268 can effectively be traced back to the high-latitude heating location on Day 267. The perturbation of thermospheric composition in this area was strongly enhanced by the large positive values of IMF  $B_y$ .

## 6.2. Day 280–281: Prolonged Activity With By Reversal

[30] A second period of interest is on Days 280–281, when the Auroral Electrojet index indicates strong magnetic activity beginning after 1000 UT on Day 280 (see Figure 2). The activity on Day 280 occurred under the influence of negative IMF  $B_y$ , followed by activity on Day 281 mainly under positive IMF  $B_y$  conditions. In a test similar to that described in the previous section, a By-reversed run of the TIMEGCM enables comparisons to the Truth run, and Figure 8 shows the differences between the two along with corresponding DE-1 FUV images at two times of interest. A PD image compiled from images obtained between 1400 UT and 1500 UT on Day 280 appears in the left panel of Figure 8a. At this time AE is rising, but the activity has been moderate, with a mean value of 255 nT in the 12 hours before imaging. That activity occurred mainly during times of IMF  $B_y < 0$ , with values approaching  $-10$  nT before 0600 UT (see Figure 2). The composition disturbance zone produced by the heating is significant, though IMF  $B_y$  only weakly influences its distribution, as shown in the By-difference plot of Figure 8a.

[31] Though IMF  $B_y$  appears to have a relatively low level of influence at this time, an enhancement of  $\sim 5\%$  in  $\Sigma\text{O}/\text{N}_2$  in the prenoon sector at middle latitudes (North America) appears in the By-reversed run, and 5% reductions

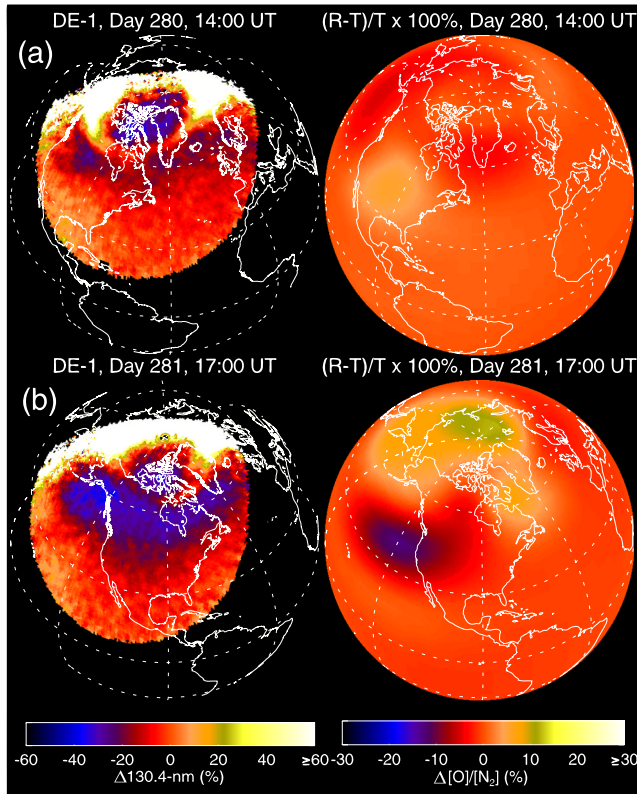


**Figure 8.** Effect of IMF-By reversal on TIMEGCM  $\Sigma O/N_2$ . Two DE-1 PD images from (a) 1500 UT on Day 280 and (b) 1700 UT on Day 281, alongside difference plots of TIMEGCM  $\Sigma O/N_2$  between the Truth and By-reversed runs.

appear in the postmidnight sector and at high latitudes near noon. At this instant in time, the Truth run represents IMF  $B_y < 0$ , as opposed to the case discussed in the preceding section. The small variations are a “negative” image of the differences seen on Day 267, when the By-reversed run produced greater decreases over North America and lesser reductions in  $\Sigma O/N_2$  in the polar cap (cf. Figure 6, 1600–2000 UT). Crowley *et al.* [2006] predict this effect.

[32] At the beginning of Day 281, the y-component of the IMF varies widely about 0 nT with two positive excursions (see Figure 2), and after 0500 UT the y-component remains positive for the remainder of the day and most of the next. During this time there are several intervals of high-latitude heating, as inferred from the AE index and as expected from the predominantly negative values of IMF  $B_z$ . The resultant perturbation in the TIMEGCM  $\Sigma O/N_2$  has a significant dependence on  $B_y$ , shown in Figure 8b. The By-reversed (here,  $B_y < 0$ ) run shows an up to 12% further reduction in  $\Sigma O/N_2$  centered off the western coast of North America, with smaller reductions in  $\Sigma O/N_2$  at high latitudes relative to the Truth run. This bears an obvious resemblance to the difference images in the bottom part of Figure 6 and presents another case in which  $B_y < 0$  (here, the By-reversed run) produces greater decreases in  $\Sigma O/N_2$  in the morning sector at middle latitudes after enhancements in magnetic activity, while  $B_y > 0$  produces more extensive decreases at high latitudes.

## 7. Comparison of Total $\Sigma O/N_2$ Perturbation in the Truth and By-Reversed TIMEGCM Runs

[33] The comparisons shown for Days 267–268 and 280–281 identify the trend toward stronger  $\Sigma O/N_2$  reductions in the middle-latitude morning sector when IMF  $B_y < 0$ , and greater high-latitude disturbances when IMF  $B_y > 0$ . This section considers the question of whether the overall thermospheric perturbation is greater under either IMF orientation.

[34] To quantify the overall perturbation, the  $\Sigma O/N_2$  PD values are determined over the entire Northern Hemisphere for each of the hourly TIMEGCM outputs. Model cells in which the negative perturbation is  $-20\%$  or stronger are identified (same as the green contour in Figures 3 and 4) and the geographic area of the cell is multiplied by the percent perturbation value therein. The Northern Hemispheric total of area\*PD is determined at each hour of the Truth and By-reversed runs as shown in Figure 9. This perturbation index quantifies the effects of magnetic activity during the two periods of interest and is called  $PD_Q$ . Mathematically, it is defined as follows:

$$PD_Q = \int^{NH} PD(A)H(PD) dA \quad \text{where} \quad (1)$$

$$H(PD) = \begin{cases} 1 & \text{for } PD \leq -20\% \\ 0 & \text{for } PD > -20\% \end{cases}$$

where A is area, and the limit NH indicates the entire Northern Hemisphere.

[35] The values of IMF  $B_y$  from Figures 1 and 2 are also shown in the two panels of Figure 9 in a histogram above the  $PD_Q$  values. The width indicates the strength of the y-component and the color indicates the sign (e.g., purple for  $B_y > 0$ ). During the Day 266–269 period, the Truth run exhibits an up to 30% larger perturbation in thermospheric composition than the By-reversed run. This is also the case on Days 279–282 though the  $PD_Q$  difference reaches only  $\sim 10\%$ . Though the percent differences are small, the larger  $PD_Q$  values consistently favor the run which is at that particular time experiencing a high latitude electric field associated with  $B_y > 0$ .

[36] The large difference in the overall perturbation of the thermosphere in the auroral zone is likely related to the difference in Joule heating. The instantaneous volume heating rate can be expressed as

$$q_j = \sigma_P (\mathbf{E}_\perp + \mathbf{u}_n \times \mathbf{B})^2. \quad (2)$$

In this expression,  $\sigma_P$  is the Pedersen conductance,  $\mathbf{E}_\perp$  is the electric field component perpendicular to  $\mathbf{B}$ , and  $\mathbf{u}_n$  is the neutral wind. The high-latitude electric field and conductance are controlled directly by the parameterized inputs, but the first-principles calculation of neutral winds provides for the determination of the total Joule heating. For comparison to the  $PD_Q$  values shown in Figure 9, we calculate the Joule heating in the Northern Hemisphere everywhere above  $40^\circ$  in 1-hour steps of the Truth and By-reversed model outputs. From these the total Hemispheric Joule heating is determined and shown for the two periods of interest in Figure 10. The result is that the difference between the Joule heating between the Truth and By-

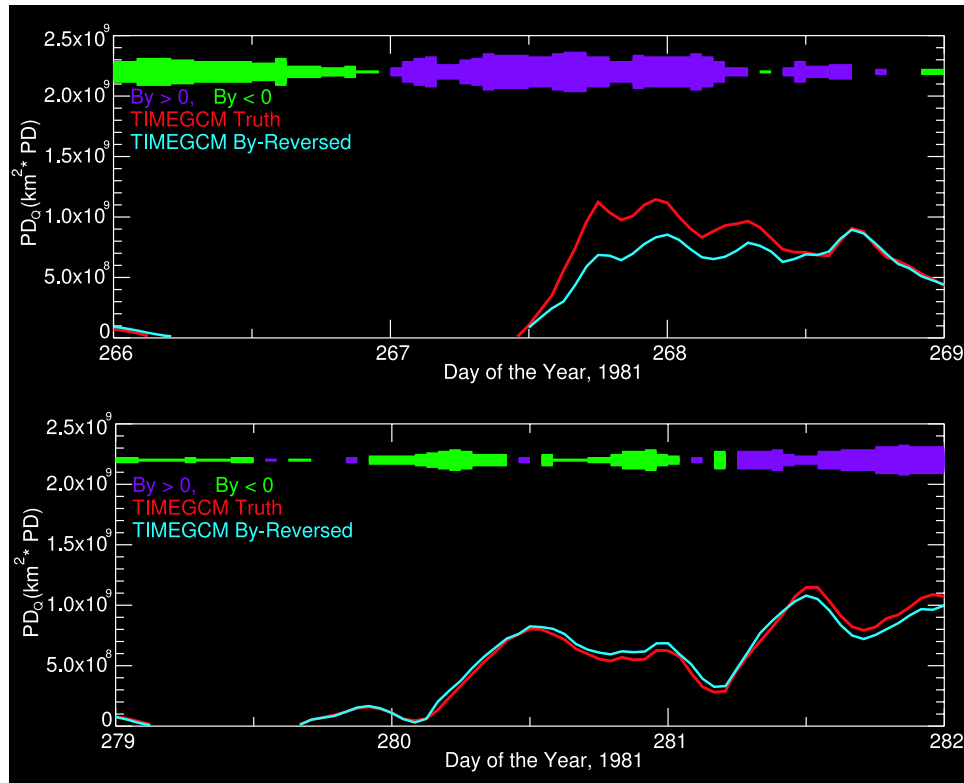


**Figure 9.** Degree of Northern Hemisphere  $\Sigma\text{O}/\text{N}_2$  perturbation in the Truth and By-reversed TIMEGCM runs for two periods of interest. The product of the area of the region of  $\Sigma\text{O}/\text{N}_2$  depletions of  $-20\%$  or greater magnitude and the perturbation percent itself is quantified ( $\text{PD}_O$ ). The figure shows this product for both TIMEGCM runs with a red (blue) trace for the Truth (By-reversed) runs. A line above the  $\text{PD}_O$  traces indicates the sign and magnitude of the y-component of the IMF. The width of the line varies with IMF  $B_y$  magnitude, and the color indicates the sign (green is negative; purple is positive).

reversed TIMEGCM runs is consistent with the degree of high-latitude thermospheric perturbation observed in the TIMEGCM  $\Sigma\text{O}/\text{N}_2$  values.

[37] The explanation for the apparent control that  $B_y$  exerts over the overall degree of Joule heating in the polar region, with up to 30% larger Northern Hemispheric heating (and subsequent thermospheric effects) with IMF  $B_y \gg 0$ , must lie in the differential motion of ions and neutrals. Neutral winds can have the effect of reducing the Joule heating rate in the lower thermosphere when oriented in the direction of the ion flow [cf. *Thayer, 1998*]. Conversely, Joule heating rates can be amplified by significant differences between ion drift and neutral winds, whether these differences are continuous or due to variations of the electric field on timescales shorter than the response time of the neutral atmosphere [*Codrescu et al., 1995; Crowley and Hackert, 2001*]. As seen in the companion paper [*Crowley et al., 2006*], for  $B_y = -7$ , the ion drifts lie along the noon-midnight meridian, while in the  $B_y = +7$  nT case the ion drifts are rotated clockwise. In the case of Day 267 where  $B_y \sim 10$  nT for many hours, the plasma channel between the convection cells is even more severely rotated. The resultant difference in Joule heating is evident in a comparison of the height integrated Joule heating pattern for the Truth and By-reversed runs at 1500 UT on Day 267, shown in Figure 11. The difference in the Joule heating patterns is evident, with a remarkable peak in heating in the polar cap

in the Truth Run, at which time  $B_y > 10$  nT. The total hemispheric heating rate at this time is 30% greater in the Truth run than the By-reversed run. The By-reversed run exhibits much lower overall heating, though with somewhat enhanced heating along the plasma channel in the polar cap.

## 8. Discussion and Conclusions

[38] In this paper, we have simulated a continuous 20-day period of thermospheric behavior during September and October 1981, for which DE-SAI images at 130.4 nm were available. While global first-principles models have frequently been validated against empirical climatologies, this study represents one of the most detailed validation studies of the TIMEGCM using realistic inputs and comparisons with two-dimensional (2-D), global-scale measurements. The DE-SAI images revealed global-scale changes in thermospheric composition caused by varying geomagnetic conditions. The TIMEGCM generated remarkably realistic simulations of these global-scale changes. We therefore proceed with an analysis of the effects of changing the high-latitude inputs with confidence.

[39] The TIMEGCM shows that geomagnetic activity occurring when IMF  $B_y < 0$  produces greater depletions in  $\Sigma\text{O}/\text{N}_2$  on the dayside at subauroral and middle latitudes in the initial 6–12 hours after the onset of activity than

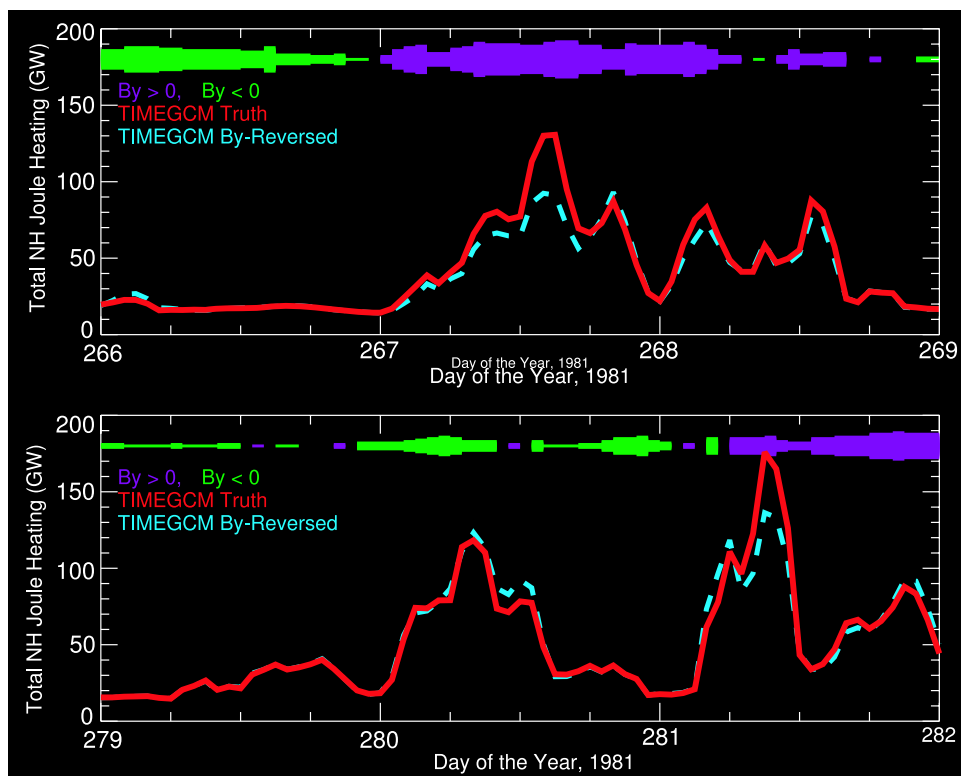


**Figure 10.** Northern Hemispheric integrated values of the total Joule heating rates are shown for the two initial periods of interest. Values from the Truth (By-Reversed) run are shown in solid red (dashed blue). The magnitude of the y-component of the IMF is indicated by the width of the bar above the plot, while the sign is indicated by its color. Day numbers along the ordinate indicate the start of the noted day.

when IMF  $B_y > 0$ . This is demonstrated in the companion paper in controlled tests [Crowley *et al.*, 2006], and here for more variable inputs. That the local time and latitude of the affected area is basically fixed with respect to the high-latitude convection suggests that this feature is dynamically maintained. A different effect is that at highest latitudes, IMF  $B_y < 0$  is associated with smaller reductions in  $\Sigma O/N_2$  than IMF  $B_y > 0$ . The relatively greater high-latitude

perturbation of  $\Sigma O/N_2$  that develops during periods of IMF  $B_y > 0$  can later migrate to middle latitudes, resulting in amplified thermospheric heating effects in the noon sector at middle latitudes more than 12 hours after the end of a particular heating event (e.g., Day 268, 1981). The composition perturbation can be 30% greater (as quantified by  $PD_Q$ ) due to an overall enhancement in Joule heating for IMF  $B_y > 0$ . Whether this difference in Joule heating is due

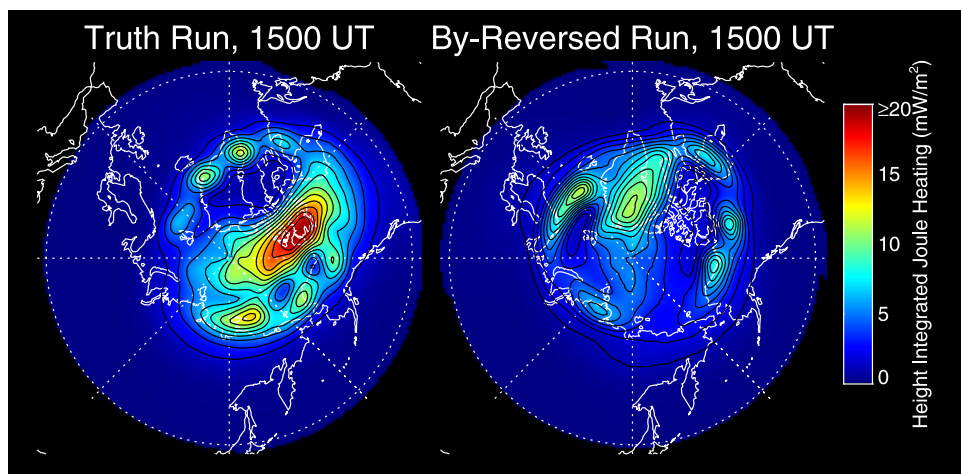


**Figure 11.** Height integrated total Joule heating determined at 1700 UT, Day 267, as determined from the TIMEGCM. The left hand figure shows the heating distribution for the Truth run, where to the right are shown the same results from the By-Reversed run.

entirely to the rotation of the cross-polar-cap plasma flow away from the noon-midnight meridian, or possibly to a shift of the high-speed flow channel between the cells across the polar cap is a question still open to investigation.

[40] *Immel et al.* [1997] concluded that the strongly positive IMF  $B_y$  on Days 267 and 281 helped produce the large dayside  $\Sigma O/N_2$  decreases observed in DE-1 images obtained on those days. The TIMEGCM results shown here do not support those conclusions, and indicate that the morning sector decrease is actually strengthened by negative IMF  $B_y$ . The simulations do help explain the inordinately large decreases seen on those days in two other ways. First, it is very clear that  $B_z$  plays a very important role in the generation of  $\Sigma O/N_2$  decreases in response to high-latitude heating and the eventual propagation of these heating effects to middle latitudes. This is particularly important when considering the earlier identification (by *Immel et al.* [1997]) of the role of IMF  $B_y$  in creating differences between FUV signatures on Days 267 and 279. That conclusion lacked a full appreciation of the importance of the difference in IMF  $B_z$  and the overall magnitude of the IMF magnetic field. Both the Truth and  $B_y$ -reversed TIMEGCM simulations show significant perturbation of  $\Sigma O/N_2$  on Day 267 (cf. Figure 9, top), while showing a minimal effect in response to the activity on Day 279 (cf. Figure 9, bottom). Similarly, in the Day 280–281 period the TIMEGCM shows a greater overall composition perturbation (cf. Figure 9) on Day 281 than Day 280, regardless of the sign of IMF  $B_y$ .

[41] Though we have begun to develop a new understanding of the IMF- $B_y$  effect on thermospheric composition, neither the persistence of the effect nor the importance of rapid changes in convection have been fully investigated. With any rotation of the convection pattern or change of relative size of the convection cells, the difference in plasma and neutral velocities will initially be large. With some time, the neutral winds will respond and to some degree conform to the new pattern of ion drifts, at which time the differential velocity term in the Joule heating equation will become less dominant. Concurrent changes in  $B_z$  will also enhance this differential-velocity component of Joule heating. This study shows there is a persistent enhancement in Joule heating with strong rotation of the convection cells away from a noon-midnight flow, but the importance of this effect when compared to a rapidly varying IMF or small-scale, high-frequency variations in the field has not been quantified here. These topics are addressed in several recent reports [cf. *Walterscheid and Brinkman*, 2003; *Aruliah et al.*, 2005; *Zhu et al.*, 2005], and will continue to be investigated using the NCAR-TIMEGCM.

[42] The IMF  $B_y$  sign represents an extremely important component in the development of middle latitude  $\Sigma O/N_2$ . The TIMEGCM model runs show that extreme values of IMF  $B_y$  during geomagnetic events have both immediate and longer lived effects at middle latitudes, driving an overall variability in  $\Sigma O/N_2$  on the order of  $\pm 30\%$  during periods of moderate geomagnetic activity. These effects can continue to propagate from high latitudes for up to 24 hours after a geomagnetic event. We believe the  $B_y$ -effect is observed in DE-SAI images on Day 268 of 1981. Modeling efforts that work on numerical grids more fine than  $5^\circ$  in latitude and longitude may produce more highly localized

Joule heating effects, particularly if they utilize high-latitude electric field models driven by assimilated data such as radar-determined ion drifts, ground-based magnetometer data, or FUV auroral images as a replacement for statistical conductance models. Also, though the TIMEGCM provides a reliable representation of the upper atmosphere and ionosphere, the effects discussed in this report should be confirmed using other first-principles models.

[43] **Acknowledgments.** This research effort was supported by NASA grant NAG5-11055. Solar wind data were provided by the National Space Science Data Center at Goddard Space Flight Center. GC and CLH were also supported by NASA Living with a Star grant NNG04GN04G, AFOSR Contract F49620-01-1-0059, NASA contract NAG-5001 to the Aerospace Corporation, and National Science Foundation grant ATM-0332307. The authors thank Eve Kushner for her contribution as an editor.

[44] Shadia Rifai Habbal thanks Rod A. Heelis and Daniel R. Weimer for their assistance in evaluating this paper.

## References

- Aruliah, A. L., et al. (2005), First direct evidence of meso-scale variability on ion-neutral dynamics using co-located tristatic FPIs and EISCAT radar in Northern Scandinavia, *Ann. Geophys.*, *23*, 147–162.
- Birkeland, K. (1913), *The Norwegian Aurora Borealis Expedition*, sect. 2, Aschehoug, Christiania, Norway.
- Burns, A. G., T. L. Killeen, W. Deng, and G. R. Carignan (1995), Geomagnetic storm effects in the low- to middle-latitude upper thermosphere, *J. Geophys. Res.*, *100*, 14,673–14,691.
- Christensen, A. B., et al. (2003), Initial observations with the Global Ultraviolet Imager (GUVI) in the NASA TIMED satellite mission, *J. Geophys. Res.*, *108*(A12), 1451, doi:10.1029/2003JA009918.
- Codrescu, M. V., T. J. Fuller-Rowell, and J. C. Foster (1995), On the importance of E-field variability for Joule heating in the high-latitude thermosphere, *Geophys. Res. Lett.*, *22*, 2393–2396.
- Conway, R. R., R. R. Meier, and R. E. Huffinan (1988), Satellite observations of the OI 1304, 1356 and 1641 Å dayglow and the abundance of atomic oxygen in the thermosphere, *Planet. Space Sci.*, *36*, 963–973.
- Craven, J. D., A. C. Nicholas, L. A. Frank, D. J. Strickland, and T. J. Immel (1994), Variations in FUV dayglow with intense auroral activity, *Geophys. Res. Lett.*, *21*, 2793–2796.
- Crowley, G., and C. L. Hackert (2001), Quantification of high latitude electric field variability, *28*, 2783–2786.
- Crowley, G., T. J. Immel, C. L. Hackert, J. D. Craven, and R. G. Roble (2006), Effect of IMF  $B_y$  on thermospheric composition at high and middle latitudes: 1. Numerical experiments, *J. Geophys. Res.*, *111*, A10311, doi:10.1029/2005JA011371.
- Drob, D. P., R. R. Meier, J. M. Picone, D. J. Strickland, R. J. Cox, and A. C. Nicholas (1999), Atomic oxygen in the thermosphere during the July 13, 1982, solar proton event deduced from far ultraviolet images, *J. Geophys. Res.*, *104*, 4267–4278.
- Frandsen, A. M. A., B. V. Connor, J. V. Amersfoort, and E. J. Smith (1978), The ISEE-C Vector Helium Magnetometer, *ISEE Trans. Geosci. Electr.*, *GE-16*, 195–198.
- Frank, L. A., and J. D. Craven (1988), Imaging results from Dynamics Explorer 1, *Rev. Geophys.*, *26*, 249–283.
- Frank, L. A., J. D. Craven, K. L. Ackerson, M. R. English, R. H. Eather, and R. L. Carovillano (1981), Global auroral imaging instrument for the Dynamic Explorer mission, *Space. Sci. Instr.*, *5*, 369.
- Fuller-Rowell, T. J., and D. S. Evans (1987), Height integrated Pedersen and Hall conductivity patterns inferred from the TIROS-NOAA satellite data, *J. Geophys. Res.*, *92*, 7606–7618.
- Gladstone, G. R. (1994), Simulations of DE 1 UV airglow images, *J. Geophys. Res.*, *99*, 11,441–11,448.
- Heelis, R. A., J. K. Lowell, and R. W. Spiro (1982), A model of the high latitude ionospheric convection pattern, *J. Geophys. Res.*, *87*, 6339–6345.
- Immel, T. J., J. D. Craven, and L. A. Frank (1997), Influence of IMF  $B_y$  on large-scale decreases of O column density at middle latitudes, *J. Atmos. Sol. Terr. Phys.*, *59*, 725–736.
- Immel, T. J., J. D. Craven, and A. C. Nicholas (2000), The DE-1 auroral imager's response to the FUV dayglow for thermospheric studies, *J. Atmos. Sol. Terr. Phys.*, *62*, 47–64.
- Immel, T. J., G. Crowley, J. D. Craven, and R. G. Roble (2001), Dayside enhancements of thermospheric  $O/N_2$  following magnetic storm onset, *J. Geophys. Res.*, *106*, 15,471–15,488.
- Jacchia, L. G. (1959), Corpuscular radiation and the acceleration of artificial satellites, *Nature*, *183*, 1662–1663.

- Meier, R. R. (1970), Depressions in the far-ultraviolet airglow over the poles, *J. Geophys. Res.*, *75*, 6218–6232.
- Meier, R. R., and D. K. Prinz (1971), Observations of the O I 1304-A airglow from Ogo 4, *J. Geophys. Res.*, *76*, 4608–4620.
- Meier, R. R., R. Cox, D. J. Strickland, J. D. Craven, and L. A. Frank (1995), Interpretation of Dynamics Explorer 1 far UV images of the quiet time thermosphere, *J. Geophys. Res.*, *100*, 5777–5794.
- Mende, S. B., H. U. Frey, T. J. Immel, J.-C. Gerard, B. Hubert, and S. A. Fuselier (2003), Global Imaging of Proton and Electron Aurorae in the far Ultraviolet, *Space Sci. Rev.*, *109*, 211–254.
- Nicholas, A. C., J. D. Craven, and L. A. Frank (1997), A survey of large-scale variations in thermospheric oxygen column density with magnetic activity as inferred from observations of the FUV dayglow, *J. Geophys. Res.*, *102*, 4493–4510.
- Parish, H. F., G. R. Gladstone, and S. Chakrabarti (1994), Interpretation of satellite airglow observations during the March 22, 1979, magnetic storm, using the coupled ionosphere-thermosphere model developed at University College, London, *J. Geophys. Res.*, *99*, 6155–6166.
- Prölss, G. W. (1980), Magnetic storm associated perturbations of the upper atmosphere: Recent results obtained by satellite-borne gas analyzers, *Rev. Geophys.*, *18*, 183–202.
- Prölss, G. W., and J. D. Craven (1998), Perturbations of the FUV dayglow and ionospheric storm effects, *Adv. Space Res.*, *22*(1).
- Prölss, G. W., and M. Roemer (1987), Thermospheric storms, *Adv. Space Res.*, *7*(10), 223–235.
- Rees, D., et al. (1986), A theoretical and empirical study of the response of the high latitude thermosphere to the sense of the “y” component of the interplanetary magnetic field, *Planet. Space Sci.*, *34*(1), 1–40.
- Roble, R. G., and E. C. Ridley (1994), A thermosphere-ionosphere-mesosphere-electro dynamics general circulation model (TIME-GCM): Equinox solar cycle minimum simulations (300–500 km), *Geophys. Res. Lett.*, *22*, 417–420.
- Strickland, D. J., and D. E. Anderson, Jr. (1977), The o i 1304 Å airglow intensity/column production rate ratio and its application to airglow studies, *J. Geophys. Res.*, *82*, 1013.
- Strickland, D. J., and G. E. Thomas (1976), Global atomic oxygen density derived from Ogo-6 1304A airglow measurements, *Planet. Space Sci.*, *24*, 313–326.
- Strickland, D. J., R. J. Cox, R. R. Meier, and D. P. Drob (1999), Global O/N<sub>2</sub> derived from DE-1 FUV dayglow data: Technique and examples from two storm periods, *J. Geophys. Res.*, *104*, 4251–4266.
- Strickland, D. J., J. D. Craven, and R. E. Daniell, Jr. (2001a), Six days of thermospheric-ionospheric weather over the Northern Hemisphere in late September 1981, *J. Geophys. Res.*, *106*, 30,291–30,306.
- Strickland, D. J., R. E. Daniell, and J. D. Craven (2001b), Negative ionospheric storm coincident with DE 1-observed thermospheric disturbance on October 14, 1981, *J. Geophys. Res.*, *106*, 21,049–21,062.
- Thayer, J. P. (1998), Height-resolved Joule heating rates in the high-latitude E region and the influence of neutral winds, *J. Geophys. Res.*, *103*, 471–487.
- Walterscheid, R. L., and D. G. Brinkman (2003), Spin-up circulation of high-latitude ion drag-driven gyres, *J. Geophys. Res.*, *108*(A7), 1304, doi:10.1029/2002JA009642.
- Zhu, X., E. R. Talaat, J. B. H. Baker, and J.-H. Yee (2005), A self-consistent derivation of ion drag and Joule heating for atmospheric dynamics in the thermosphere, *Ann. Geophys.*, *23*, 3313–3322.

---

J. D. Craven, Geophysical Institute, University of Alaska Fairbanks, Fairbanks, AK 99775-7320, USA.

G. Crowley and C. L. Hackert, ASTRA, 12703 Spectra Drive, Suite 101, San Antonio, TX 78249, USA.

T. J. Immel, Space Sciences Laboratory, University of California, Berkeley, CA 94720-7450, USA. (immel@ssl.berkeley.edu)

R. G. Roble, National Center for Atmospheric Research, Boulder, CO, USA.